

# Function-on-Function Regression for the Identification of Epigenetic Regions Exhibiting Windows of Susceptibility to Environmental Exposures

Michele Zemlenyi\*    Mark J. Meyer†    Andres Cardenas‡    Marie-France Hivert§¶  
 Sheryl L. Rifas-Shiman§    Heike Gibson||    Itai Kloog\*\*    Joel Schwartz||††  
 Emily Oken§    Dawn L. DeMeo‡‡    Diane R. Gold||††    Brent A. Coull\*

December 17, 2019

## Abstract

The ability to identify time periods when individuals are most susceptible to exposures, as well as the biological mechanisms through which these exposures act, is of great public health interest. Growing evidence supports an association between prenatal exposure to air pollution and epigenetic marks, such as DNA methylation, but the timing and gene-specific effects of these epigenetic changes are not well understood. Here, we present the first study that aims to identify prenatal windows of susceptibility to air pollution exposures in cord blood DNA methylation. In particular, we propose a function-on-function regression model that leverages data from nearby DNA methylation probes to identify epigenetic regions that exhibit windows of susceptibility to ambient particulate matter less than 2.5 microns (PM<sub>2.5</sub>). By incorporating the covariance structure among both the multivariate DNA methylation outcome and the time-varying exposure under study, this framework yields greater power to detect windows of susceptibility and greater control of false discoveries than methods that model probes independently. We compare our method to a distributed lag model approach that models DNA methylation in a probe-by-probe manner, both in simulation and by application to motivating data from the Project Viva birth cohort. In two epigenetic regions selected based on prior studies of air pollution effects on epigenome-wide methylation, we identify windows of susceptibility to PM<sub>2.5</sub> exposure near the beginning and middle of the third trimester of pregnancy.

**Keywords:** functional data analysis, wavelet regression, windows of susceptibility, epigenetics

\*Department of Biostatistics, Harvard T.H. Chan School of Public Health, Boston, Massachusetts, USA

†Department of Mathematics and Statistics, Georgetown University, Washington D.C., USA

‡Division of Environmental Health Sciences, School of Public Health, University of California, Berkeley, California, USA

§Division of Chronic Disease Research Across the Lifecourse, Department of Population Medicine, Harvard Medical School and Harvard Pilgrim Health Care Institute, Boston, Massachusetts, USA

¶Diabetes Unit, Massachusetts General Hospital, Boston, Massachusetts, USA

||Department of Environmental Health, Harvard T.H. Chan School of Public Health, Boston, Massachusetts

\*\*Department of Geography and Environmental Development, Faculty of Humanities and Social Sciences, Ben-Gurion University, Beer-Sheva, Israel

††Channing Division of Network Medicine, Department of Medicine, Brigham and Womens Hospital, Harvard Medical School, Boston, Massachusetts, USA

‡‡Center for Chest Diseases, Brigham and Women's Hospital, Boston, Massachusetts, USA

*Please address correspondence to Michele Zemlenyi; email: mzemlenyi@g.harvard.edu.*

# 1 Introduction

Recent epidemiological evidence supports the hypothesis that exposures during fetal development and in early life can lead to a variety of adverse birth and child health outcomes. The fetal *in utero* environment can be altered by external factors such as the mother’s diet or toxins to which she is exposed, thereby influencing the early development of a child at a time of heightened susceptibility. The National Institutes of Health, through its 2016 Environmental influences on Child Health Outcomes (ECHO) initiative, highlighted the importance of not only identifying child health outcomes associated with environmental exposures, but also of identifying sensitive developmental windows during which an exposure has increased association with a child’s health outcomes. Understanding when these windows of susceptibility occur and how they coincide with environmental exposures may shed light on the underlying biological pathways through which exposures act. Ultimately, this can lead to the development of interventions that mitigate risks due to an exposure.

One proposed biological pathway by which prenatal exposures could contribute to subsequent adverse health outcomes involves DNA methylation at cytosine-phosphate-guanine (CpG) sites. DNA methylation is an epigenetic modification that can regulate gene expression. Previous studies have found associations between DNA methylation levels and environmental exposures such as particulate air pollution (Gruzieva et al., 2019; Soberanes et al., 2012; Baccarelli et al., 2009) and lead (Bollati et al., 2010; Schneider et al., 2013). Lee et al. [2018] found evidence linking *in utero* PM<sub>2.5</sub> exposure to both hypermethylation of the *GSTP1* gene in nasal epithelia and impaired early childhood lung function. In a cohort of elderly men in the Normative Aging Study, Lepeule et al. [2012] found an association between lower DNA methylation levels in several gene promoter regions and reduced lung function. While a large number of epigenetic studies based on adult populations have been published, due to the inherent difficulties and health risks of interrogating the epigenome of a developing child, relatively few prenatal epigenetic studies have been conducted. Thus, our understanding of which prenatal exposures affect the epigenome, which epigenetic regions are affected, and which time periods are most sensitive remains limited.

Previous work to identify windows of susceptibility during pregnancy often involved regressing the outcome of interest on trimester-average exposures (TAEs). Either separate models for each of the three TAEs were fit, or a single model that jointly estimated the associations for each TAE was constructed (Shah and Balkhair, 2011; Dadvand et al., 2013). However, Wilson et al. [2017] demonstrated that trimester-specific effect estimates obtained using separate regression models can be biased and identify incorrect windows of susceptibility. Wilson et al. [2017] showed that, while a joint model suffers less from these issues, a distributed lag model (DLM) significantly outperforms either of the TAE methods in this regard. A DLM models the association between an outcome and a finely sampled time-varying exposure by assuming that their relationship varies smoothly over time (Schwartz, 2000; Zanobetti et al., 2000). In the context of prenatal exposure, the DLM regresses a health outcome measured after the exposure period of interest against exposure measured at frequent, regular intervals throughout pregnancy. DLMs have been used to identify windows of susceptibility during which air pollution is associated with disrupted neurodevelopment (Chiu et al., 2016), childhood asthma (Lavigne et al., 2019; Bose et al., 2017; Hsu et al., 2015), reduced lung function (Bose et al., 2018), sleep disruption (Bose et al., 2019), and lower birth weights (Wu et al., 2018; Darrow et al., 2011). Warren et al. [2019] recently proposed critical window variable selection as an alternative to the DLM in the context of identifying windows during pregnancy when PM<sub>2.5</sub> is associated with an increased risk of preterm birth.

While DLMs and methods like critical window variable selection efficiently model the multivariate nature of exposure, further efficiency gains can be made by taking into account the dependence among multivariate outcomes. In mammalian genomes, DNA methyltransferase enzymes can co-methylate adjacent CpG sites, resulting in blocks of CpG sites with similar methylation statuses and genomic functionality (Guo et al., 2017). Lee et al. [2017] proposed a Bayesian variable selection method for multivariate methylation outcomes that, through leveraging information on the covariance structure of outcomes, increases power to detect associations while maintaining a low false discovery rate. Additionally, Lee and Morris [2016] used the wavelet-based functional mixed model approach introduced by Morris and Carroll [2006] to model DNA methylation outcomes jointly, thereby capturing correlations among neighboring probes as well as across samples. This yielded gains in efficiency and the ability to detect differentially methylated regions (DMRs).

Lee and Morris [2016] focused on detecting DMRs associated with a scalar exposure, such as cancer status. Here, we consider the functional exposure setting where our goal is not only to find DMRs, but to

simultaneously identify time periods during which an exposure is associated with these DMRs. In particular, we are interested in the association between two functions: 1) cord-blood DNA methylation levels measured at birth as a function of CpG site position in the genome, and 2) maternal air pollution exposure as a function of time during pregnancy. To characterize the association surface between these two functions, we propose the use of Bayesian function-on-function regression (FFR), a recent extension of Morris and Carroll’s [2006] wavelet-based functional model developed by Meyer et al. [2015]. FFR transforms both the DNA methylation and air pollution profiles to a basis space, fits a regression model in that space, and then performs an inverse transformation to present results on the original methylation scale. The basis transformation affords the ability to capture spatial and time-varying correlations within the two functions, while the Bayesian approach simultaneously allows for the smoothing of the association surface via the prior specification as well as strict control for multiple testing.

We fit the model using a Monte-Carlo Markov Chain (MCMC) procedure and then perform statistical inference while accounting for multiple testing using a Bayesian False Discovery Rate (BFDR) procedure for functional regression and a simultaneous band score (SimBaS) (Meyer et al., 2015). We demonstrate the efficiency gains and better control of false discoveries attained by the functional approach relative to DLMS applied on a site-by-site basis in simulation. We then take two biologically-interesting and significant sites reported in Gruzieva et al., 2019, the largest analysis to date of particulate matter exposure and DNA methylation in infants, and perform the first analysis of prenatal windows of susceptibility driving these associations. We perform the analysis using DNA methylation data from 412 mother-child pairs enrolled in the Project Viva birth cohort and daily PM<sub>2.5</sub> measurements recorded over the third trimester of pregnancy, a critical period in fetal somatic growth, as well as in neural, lung, endocrine, and immune system development (Hill, 2019). We identify two windows of susceptibility for CpG probes in the *FAM13A* gene region and another window of susceptibility in the third trimester for a subset of CpG probes in the *NOTCH4* region. While we present the functional model in the context of a specific outcome measure (DNA methylation) and exposure (air pollution), the method is flexible enough to analyze other types of outcome and predictor functions that vary spatially and/or temporally.

## 2 Methylation and Exposure Data in Project Viva

In this section we briefly describe the pre-birth cohort, DNA methylation data, and air pollution data sets to which we apply our method.

### 2.1 Description of Project Viva

Project Viva is a longitudinal study designed to examine the effect of maternal diet and other lifestyle factors during pregnancy on the mother’s and child’s health. Pregnant women were enrolled at their initial obstetric visit at Harvard Vanguard Medical Associates in Massachusetts from 1999-2002. Of the 2,128 mother-child pairs enrolled in the cohort, 485 had cord blood DNA methylation measurements that passed quality control. For a more detailed description of the Project Viva cohort see Oken et al. [2015].

### 2.2 DNA methylation data

Umbilical vein cord blood DNA was extracted using the Qiagen Puregene Kit (Valencia, CA) and bisulfite converted using the EZ DNA Methylation-Gold Kit (Zymo Research, Irvine, CA). Samples were randomly allocated to chips and plates and analyzed using Infinium HumanMethylation450 BeadChip arrays (Illumina, San Diego, CA) that probe approximately 485,000 CpG sites at a single nucleotide resolution.

We adjusted for sample plate as technical batch by directly including the batch number as a scalar covariate in the FFR and DLM regression models. We modelled the logit-transformed percentage DNA methylation value, or M-values, where the percentage methylation value for an individual CpG site is the percentage of methylated cytosines over the sum of methylated and un-methylated cytosines at the 5C position for that probe (Du et al., 2010).

We focused our analysis on two regions encompassing CpG sites identified in closely related work by Gruzieva et al., 2019. From their meta-analysis of the associations between prenatal exposure to particulate matter and DNA methylation in nine birth cohorts, one of which was Project Viva, Gruzieva et al., 2019

identified 20 CpGs that were significantly associated with either prenatal PM<sub>2.5</sub> or PM<sub>10</sub> exposure. Two of these CpGs mapped to *FAM13A* and *NOTCH4*, genes previously associated with COPD and asthma, respectively (Hobbs et al., 2017; Hancock et al., 2009; Li et al., 2013). We selected CpG probes annotated to these two genes for our analysis.

### 2.3 PM<sub>2.5</sub> data

Particulate matter with diameter less than 2.5  $\mu\text{m}$  (PM<sub>2.5</sub>) is released by vehicles and other industrial processes via the combustion of solid and liquid fuels. Estimated daily ambient PM<sub>2.5</sub> levels at the home addresses of the mothers enrolled in Project Viva were obtained using a hybrid satellite-based model that integrated remote sensing data and spatio-temporal land-use and meteorology data (Kloog et al., 2011; Kloog et al., 2014). In Project Viva we have demonstrated associations of estimated residential third trimester PM<sub>2.5</sub> or its black carbon component with subsequent reduced fetal growth measures at birth (Fleisch et al., 2015); childhood executive function and behavior (Harris et al., 2016); and allergen sensitization (Sordillo et al., 2019). Since recruiting for Project Viva began in 1999, but the satellite technology necessary to make daily predictions only became available in 2000, we do not have complete daily 1-by-1 km-resolved PM<sub>2.5</sub> exposure estimates throughout pregnancy for all mother-child pairs. Because of the known importance of the third trimester in fetal development, and in the interest of retaining a large number of subjects, we limited analysis to the 412 mothers for whom we had daily PM<sub>2.5</sub> measurements at their residential addresses for the last 90 days prior to delivery. While analyzing the entirety of gestation would be preferable, exploring the last trimester of pregnancy does not preclude us from finding biologically meaningful windows of susceptibility; previous studies have found associations between prenatal air pollution in the third trimester and newborn health outcomes such as systolic blood pressure (van Rossem et al., 2015) and fetal growth (Lamichhane et al., 2018).

## 3 Methods

### 3.1 Function-on-Function regression model

Here, we describe the FFR model introduced by Meyer et al. (2015) in the context of identifying regions of the genome that exhibit windows of susceptibility to an exposure of interest. Suppose for each of  $i = 1, \dots, n$  individuals we observe two functions: (1) the DNA methylation profile  $y_i(s)$  on a common grid of CpG sites  $s = 1, \dots, S$ , and (2) the air pollution exposure profile over time,  $x_i(t)$ ,  $t = 1, \dots, T$ . For our application,  $x_i(t)$  represents daily ambient PM<sub>2.5</sub> levels at each mother’s residence.

A FFR model to regress  $y_i(s)$  on the functional predictor  $x_i(t)$  is given by

$$y_i(s) = \alpha(s) + \int_{t \in T} x_i(t) \beta(t, s) dt + e_i(s), \quad (1)$$

where we assume observation-specific Gaussian process errors  $e_i(s) \sim \mathcal{GP}(0, \Sigma_e)$ . The target of interest in Model (1) is the two-dimensional surface  $\beta(t, s)$  that characterizes the association between exposure at any given time and DNA methylation at any given CpG site.

If we stack row vectors by subject, then  $\mathbf{Y}$  and  $\mathbf{X}$  represent  $n \times S$  and  $n \times T$  matrices of observed DNA methylation and exposure profiles respectively. We can then represent Model (1) in matrix form as

$$\mathbf{Y} = \mathbf{X}\boldsymbol{\beta} + \mathbf{E}, \quad (2)$$

where  $\boldsymbol{\beta}$  is a  $T \times S$  matrix of functional effects and  $\mathbf{E}$  is a  $n \times S$  matrix of model errors. The intercept  $\alpha(s)$  can be incorporated into  $\boldsymbol{\beta}$ , but in practice and without loss of generality, we center and scale both  $y_i(s)$  and  $x_i(t)$  such that  $\alpha(s)$  is zero in Model 1.

One possible approach to fitting Model (2) is to fit each column of  $\mathbf{Y}$  independently using a DLM. This approach regresses DNA methylation at a particular CpG site against lagged exposure values over time for each site  $s$  separately:

$$y_{i,s} = \alpha + \int_{t \in T} x_i(t) \beta(t) dt + e_i. \quad (3)$$

This site-by-site DLM approach fails to borrow information across nearby, correlated CpG sites, likely reducing the efficiency of the method relative to a joint approach. Instead, we fit Model (2) jointly by using a basis function transform approach (Lee and Morris, 2016; Meyer et al., 2015; Morris and Carroll, 2006). This involves first transforming  $y(s)$  and  $x(t)$  from the data space into a basis space. We fit the model in the basis space and then transform the parameter estimates back to the data space to conduct inference.

### 3.2 Discrete Wavelet Transform in Functional Regression

While a number of basis functions could be used to represent the observed functions, including splines, principal components (PCs), or Fourier series, we use wavelets as the transformation for both the DNA methylation and air pollution datasets. Wavelets have previously been used in genomic settings for the purposes of denoising high-throughput DNA copy number data (Hsu et al., 2005), detecting histone modification enrichments (Mitra and Song, 2012), and identifying nucleosome position (Nguyen et al., 2013). For equally spaced data, such as daily air pollution measurements, the discrete wavelet transform (DWT) maps the data to the wavelet space in linear time. For unequally spaced data, like CpG site positions across chromosomes, we have a choice for how to perform the wavelet basis transform. We choose to perform the transformation treating the positions as if they were equally spaced for two reasons. First, Morris and Carroll [2006] showed that the wavelet-based functional mixed model can flexibly estimate a complex covariance structure such as one that might arise from unequally spaced measurements. Second, Sardy et al. [1999] compared four different approaches for handling unequally spaced data and found that the method that treats data as if it were evenly spaced performed as well as more computationally-expensive methods that account for unequal spacing. Therefore, we proceed by treating CpG sites as if they were equally spaced as others have previously done for CpG site (Lee and Morris, 2016) and DNA copy number data (Hsu et al. [2015]).

First, we apply the discrete wavelet transform (DWT) to each row of  $\mathbf{Y}$ , giving an  $n \times S^*$  matrix of wavelet basis coefficients,  $\mathbf{Y}^*$ , which represents the methylation data in the wavelet space. Each wavelet coefficient is double-indexed by  $(j, k)$  with frequencies indexed by  $j$  and locations indexed by  $k$ . For the exposure data we similarly perform the DWT on each row of  $\mathbf{X}$ , giving an  $n \times T^*$  matrix  $\mathbf{X}^*$ . Applying the DWT to  $\mathbf{Y}$  is equivalent to post-multiplication by the  $S \times S^*$  wavelet transform matrix  $\mathbf{\Omega}'$ ,  $\mathbf{Y}^* = \mathbf{Y}\mathbf{\Omega}'$ , where  $\mathbf{\Omega}'$  contains the wavelet basis functions evaluated on the grid  $S$ . Similarly, if the  $T \times T^*$  matrix  $\mathbf{\Phi}'$  contains the wavelet basis functions evaluated on the grid  $T$ , then applying the DWT to  $\mathbf{X}$  is equivalent to  $\mathbf{X}^* = \mathbf{X}\mathbf{\Phi}'$ .

Our transformation strategy differs slightly from earlier implementations. Since dimension reduction in  $\mathbf{X}^*$  has important computational benefits, others have performed an additional PCA step on the wavelet space exposure data before fitting the model [Meyer et al., 2015]. However, we forego the computational advantage of compressing the exposure data since simulations showed that compression can distort the signal in certain areas of the association surface for our setting.

After transforming both the response and exposure data, we arrive at our model in the wavelet space:

$$\mathbf{Y}^* = \mathbf{X}^*\boldsymbol{\beta}^* + \mathbf{E}^*, \quad (4)$$

where  $\mathbf{E}^* \sim \mathcal{MN}(\mathbf{0}, \mathbf{I}, \mathbf{C}^*)$  and  $\mathbf{I}$  is the appropriately sized identity matrix. The whitening property of the wavelet transform, discussed in Johnstone and Silverman [1997], allows us to assume that wavelet coefficients within a given curve are independent across  $j$  and  $k$ . Thus, we assume a diagonal structure for  $\mathbf{C}^*$ , the between-column covariance of the methylation data in the wavelet space (Morris and Carroll, 2006). Importantly, this assumed independence in the wavelet space does not imply independence in the data space; in fact, heterogeneous variances across the wavelet scales and locations  $(j, k)$  induce correlations in the data space (Morris and Carroll, 2006).

The independence assumption in the wavelet space allows us to view Model (4) as  $S^*$  separate models, one for each column of  $\mathbf{Y}^*$ . Thus, the model for each column (equivalently, Y-space wavelet coefficient) is

$$\mathbf{y}^*_{(j,k)} = \mathbf{X}^*\boldsymbol{\beta}^*_{(j,k)} + \mathbf{e}^*_{(j,k)}, \quad (5)$$

where  $\mathbf{y}^*_{(j,k)}$  and  $\mathbf{e}^*_{(j,k)}$  are  $n \times 1$ ,  $\mathbf{X}^*$  is  $n \times T^*$ , and  $\boldsymbol{\beta}^*_{(j,k)}$  is  $T^* \times 1$ . We fit Model (5) in a similar fashion to Meyer et al. [2015]. We place a spike-and-slab prior on each  $\beta^*_{(p,j,k)}$ , where  $p$  indexes the wavelet coefficients of the transformed exposure data,  $p = 1, \dots, T^*$ :

$$\beta^*_{(p,j,k)} \sim \gamma_{(p,j,k)}\mathcal{N}(0, \tau_{p,j}) + (1 - \gamma_{(p,j,k)})d_0, \quad \gamma_{(p,j,k)} \sim \text{Bern}(\pi_{p,j}). \quad (6)$$

This prior is a mixture of a normal distribution and a point-mass at zero,  $d_0$ , with regularization parameters  $\tau_{p,j}$  and  $\pi_{p,j}$  estimated using an Empirical Bayes-type approach. This prior specification is consistent with other wavelet-based functional models (Morris and Carroll, 2006; Malloy et al., 2010).

We generate posterior samples for the coefficient surface  $\beta^*$  in the wavelet space and then project back to the data space through two inverse discrete wavelet transforms,  $\beta = \Phi' \beta^* \Omega$ , which ultimately yields posterior samples of the discretized coefficient surface  $\beta$ . We then perform inference on  $\beta$  as described in Section 2.4. We perform computations in MATLAB (version 2017a). Code for running the above model will be available soon through the BayesFMM Github repository.

### 3.3 Incorporation of Scalar Covariates

Model (1) can be extended to include scalar covariates, scalar-by-function interactions, and subject-specific random effect functions [Meyer et al., 2015]. In the Viva analysis, we adjust for scalar covariates  $\{w_a, a = 1, \dots, q\}$  using

$$y_i(s) = \alpha(s) + \sum_{a=1}^q w_{ia} \gamma_a(s) + \int_{t \in T} x_i(t) \beta(t, s) dt + e_i(s), \quad (7)$$

where  $\gamma_a(s)$  are functional coefficients for scalar predictors. These coefficients are typically of less interest than the coefficient surface  $\beta(t, s)$ . Because they are not functional data, we do not transform scalar covariates into the wavelet space prior to fitting the model.

### 3.4 Posterior Functional Inference

In order to account for the multiple comparisons that occur when testing coefficients corresponding to all sites and exposure times within an analysis, we use two posterior functional inference procedures. The first is the Bayesian false discovery rate (BFDR), which was originally proposed by Müller et al. [2006] and subsequently extended to the functional regression setting (Morris et al., 2008; Malloy et al., 2010; Meyer et al., 2015). The second approach uses joint credible bands to detect significantly differentially methylated loci while controlling the experiment-wise error rate (Meyer et al., 2015).

#### 3.4.1 Bayesian FDR

Interest focuses on detecting a biologically meaningful effect size of at least  $\delta$ . For  $M$  MCMC samples, let  $\beta^{(m)}(t, s)$  be one posterior sample of the coefficient surface for sample  $m$ ,  $m = 1, \dots, M$ . We can compute the point-wise posterior probability of a  $\delta$ -sized intensity change on the  $T \times S$  grid determined by each time-point  $t = 1, \dots, T$  and genomic loci  $s = 1, \dots, S$  via

$$p(t, s) = Pr\{|\beta(t, s)| > \delta | \mathbf{Y}\} \approx \frac{1}{M} \sum_{m=1}^M I\{|\beta^{(m)}(t, s)| > \delta\},$$

where  $I$  is the indicator function. High values of  $p(t, s)$  provide stronger evidence for a true discovery at a specific point on the surface; correspondingly, the quantity  $1 - p(t, s)$  can be interpreted as a local false discovery rate at a given location (Morris et al., 2008). A location on the coefficient surface is flagged as significant if  $p(t, s) > \nu_\alpha$ , where  $\nu_\alpha$  is a threshold and  $\alpha$  is a pre-specified global FDR-bound. The threshold  $\nu_\alpha$  is constructed such that on average we expect at most  $\alpha$  percent of flagged sites to be false positives. We do this by first sorting  $\{p(t, s), t = 1, \dots, T, s = 1, \dots, S\}$  in descending order across all locations to obtain  $\{p_{(r)}, r = 1, \dots, R\}$ , where  $R = TS$ . We then define  $\lambda = \max\{r^* : \frac{1}{r^*} \sum_{r=1}^{r^*} (1 - p_{(r)}) \leq \alpha\}$  and set the cutoff for flagging significant coefficients as  $\nu_\alpha = p_{(\lambda)}$ .

#### 3.4.2 Joint Credible Bands and Simultaneous Band Scores

In applications where there is not consensus on a biologically meaningful value for  $\delta$ , it is useful to consider constructing joint credible bands. Joint credible bands have the benefit of not requiring specification of  $\delta$ ,

while still providing a means of controlling the experiment-wise error rate. A  $100(1 - \alpha)\%$  credible band of  $\beta(t, s)$  must satisfy

$$Pr\{L(t, s) \leq \beta(t, s) \leq U(t, s) \forall t \in T, s \in S\} \geq 1 - \alpha, \quad (8)$$

where  $L(t, s)$  and  $U(t, s)$  are the lower and upper bounds of the band respectively (Ruppert, 2003). If we assume approximate normality of the posterior samples, an interval satisfying this constraint is

$$I_\alpha(t, s) = \hat{\beta}(t, s) \pm q_{(1-\alpha)}[SD\{\hat{\beta}(t, s)\}]. \quad (9)$$

Here,  $\hat{\beta}(t, s)$  is the mean for a given position  $(t, s)$  taken over all  $M$  MCMC samples and  $SD\{\hat{\beta}(t, s)\}$  is the standard deviation over all  $M$  MCMC samples divided by the factor  $A(M, \rho_{MCMC})$ , where  $\rho_{MCMC}$  is an estimate of the lag autocorrelation in the samples, and  $A$  is the bias correction factor described in Anderson [1971] (Meyer et al., 2015; Lee and Morris, 2016). The variable  $q_{(1-\alpha)}$  is the  $(1 - \alpha)$  sample quantile taken over  $M$  samples of

$$Z^{(m)} = \max_{t \in T, s \in S} \left| \frac{\beta^{(m)}(t, s) - \hat{\beta}(t, s)}{SD\{\hat{\beta}(t, s)\}} \right|. \quad (10)$$

Suppose one constructs joint credible bands for a range of different values of  $\alpha$  and finds for each location  $(t, s)$  the minimum level  $\alpha$  for which the  $(1 - \alpha)\%$  joint credible band excludes zero. Meyer et al. [2015] refers to this minimum  $\alpha$  level,  $p_{SimBaS}(t, s) = \min\{\alpha : 0 \notin I_\alpha(t, s)\}$ , as the simultaneous band score (SimBaS) for each location  $(t, s)$ . For any specific  $\alpha$ , we flag all  $(t, s)$  for which  $p_{SimBaS}(t, s) < \alpha$  as significant, meaning that the  $(1 - \alpha)\%$  joint credible interval at those locations does not include zero.

## 4 Simulation

We performed two simulation studies to compare the operating characteristics of the FFR and site-by-site DLM approaches in the context of pre-birth studies of air pollution and DNA methylation. For the first study, we set the true surface of association,  $\beta$ , over a  $T = 90$  by  $S = 100$  grid to be  $\beta = 0.2$  in the region  $T \times S = \{(T, S) : T \in \{40, \dots, 44\}, S \in \{1, \dots, 100\}\}$  and  $\beta = 0$  everywhere else. This corresponds to a “vertical band” of association (Figure 1) representing a biologically plausible association between air pollution exposure and DNA methylation in which changes in air pollution halfway through the study period are associated with changes in DNA methylation in a genomic region spanning 100 CpG sites. Next, we randomly sampled  $PM_{2.5}$  pollutant profiles from individuals in the Project Viva cohort and used these randomly sampled profiles as the exposure curves  $\mathbf{x}_i$ . Motivated by the 412 mother-child pairs for whom we had data in the Project Viva cohort, we used a sample size of  $N = 400$  subjects for the simulations. Using measured exposure data, instead of simulating exposure curves, allowed us to capture a realistic correlation structure among daily pollutant exposures during pregnancy. (See the Appendix for a sample of the observed  $PM_{2.5}$  exposure curves used in the simulation study and data application.) We then generated response curves  $\mathbf{y}_i$  using  $\mathbf{y}_i = \mathbf{x}_i\beta + \mathbf{e}_i$ , where  $\mathbf{y}_i$  is a row vector of length 100,  $\mathbf{x}_i$  is a row vector of length 90,  $\beta$  is the  $90 \times 100$  matrix described above, and  $\mathbf{e}_i$  is a row vector of length 100. For the model errors  $\mathbf{e}_i$ , we generated data using Gaussian Processes with auto-regressive 1 covariance structures which were then scaled by factors of  $\sigma_e^2 \in \{4, 16, 64\}$  to create three scenarios of varying noise levels. We defined the signal-to-noise ratio, STNR, as the pointwise effect in the non-zero region of the surface ( $\beta = 0.2$ ) expressed as a proportion of  $\sigma_e$ . Using this definition, the three STNRs we considered were  $STNR \in \{0.10, 0.05, 0.025\}$ .

For each scenario, we generated 100 simulated data sets and fit the FFR to obtain 100  $\hat{\beta}_{FFR}$  estimates of the association surface. To fit the models, we transformed the data to the wavelet space using Daubechies wavelets with six levels of decomposition, four vanishing moments, and zero-padding. We drew 2000 posterior samples and discarded the first 1000 samples.

Fitting the site-by-site DLM to the simulated data sets required additional steps. Recall that the FFR takes a functional response and functional exposure as inputs and estimates a two-dimensional surface of association,  $\beta(t, s)$ , whereas the DLM takes a scalar response and functional exposure as inputs and estimates a curve of association  $\beta(t)$  for each site. To compare the FFR and DLM approaches, we fit separate DLMs for each of the  $S = 1, \dots, 100$  probes and concatenated the results, in essence stacking the DLM-estimated curves one behind the other to create a surface,  $\hat{\beta}_{DLM}$ , analogous to the FFR-estimated surface,  $\hat{\beta}_{FFR}$ . We

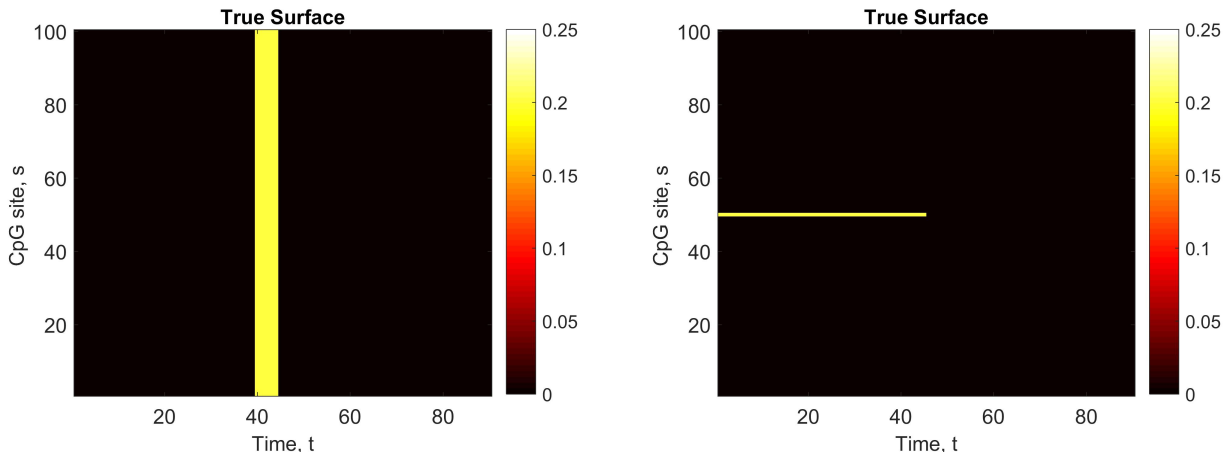


Figure 1: True association surfaces  $\beta$ . Left: vertical band setting where  $\beta = 0.2$  in the region  $T \times S = \{(T, S) : T \in \{40, \dots, 44\}, S \in \{1, \dots, 100\}\}$  and  $\beta = 0$  everywhere else. Right: horizontal band setting where  $\beta = 0.2$  in the region  $T \times S = \{(T, S) : T \in \{1, \dots, 45\}, S = 50\}$  and  $\beta = 0$  everywhere else.

used the `regimes` R package to fit the DLMS. Note that the key difference between  $\hat{\beta}_{\text{FFR}}$  and  $\hat{\beta}_{\text{DLM}}$  is that we fit  $\hat{\beta}_{\text{FFR}}$  using information from all sites simultaneously, whereas we constructed  $\hat{\beta}_{\text{DLM}}$  using a separate model fit for each site. Figure 2 displays heat maps of the estimated association surfaces for both methods across the three STNR scenarios. Results for the estimated surfaces averaged over 100 datasets can be found in the Appendix.

Figure 2 shows that both methods estimated the true surface relatively well even in situations where the magnitude of the noise was 10-40 times larger than that of  $\beta$  in the signal region. However, visually we see that FFR produced sharper estimates of the association surface. In particular, the edges of the vertical band are clearly delineated and the null region is more accurately estimated in the FFR heat maps than in the DLM heat maps.

Figure 3 shows the root mean square error (RMSE) for all scenarios. The site-by-site DLM estimates had higher RMSE throughout the surface at each STNR level. Relative to the site-by-site DLM analysis, the FFR method reduced the sum of the RMSE over the entire surface by 68%, 63%, and 65% for the STNR = 0.10, 0.05, and 0.025 scenarios, respectively. The null regions saw the largest gains in efficiency from the joint approach, while the top and bottom edges of the region of interest had the smallest gains. These differences in efficiency gains are due to the fact that spatial smoothing is less effective for sites at the boundary of the signal region. Sites in the interior of the region borrow information from a greater number of sites and therefore gain more from a joint-modeling approach.

We also compared the performance of the BFDR and SimBaS inferential procedures for the two methods, using  $\alpha = 0.05$  to select significant locations for both procedures. For the BFDR, we used  $\delta$ -intensity changes of 0.15, 0.10, and 0.05 corresponding to 75%, 50% and 25% of the true signal in the vertical band. We performed BFDR and SimBaS procedures on each estimated surface and then averaged over simulations. The heat maps in Figure 4 are shaded according to the proportion of simulations in which each location was flagged as significant by the BFDR procedure. Figure 4 shows heat maps for the STNR = 0.10 scenario across the three  $\delta$  levels. Locations that were flagged as significant by all simulations are white, those that were never flagged are black, and locations that were occasionally flagged vary from red to yellow shading. The accompanying Table 1 displays the sensitivity and false discovery rate, FDR, for both methods at varying  $\delta$  levels. Across  $\delta$  levels, FFR performed well, flagging regions with a true signal as significant in all estimated surfaces, while maintaining a FDR below 5%. This does not hold true for the DLM method. At  $\delta = 0.15$ , BFDR only flagged 66% of the vertical band as significant, while at  $\delta = 0.05$ , the method flagged too many locations neighboring the true band as significant, pushing the FDR to 30%.

Figure 5 shows heat maps obtained by averaging the SimBaS for each location over all simulations and then flagging locations with scores  $\leq 0.05$  in white. Similar to the BFDR results, at STNR = 0.10, FFR outperformed DLM by maintaining high sensitivity and low FDR, while the DLM had a high FDR of 29%.



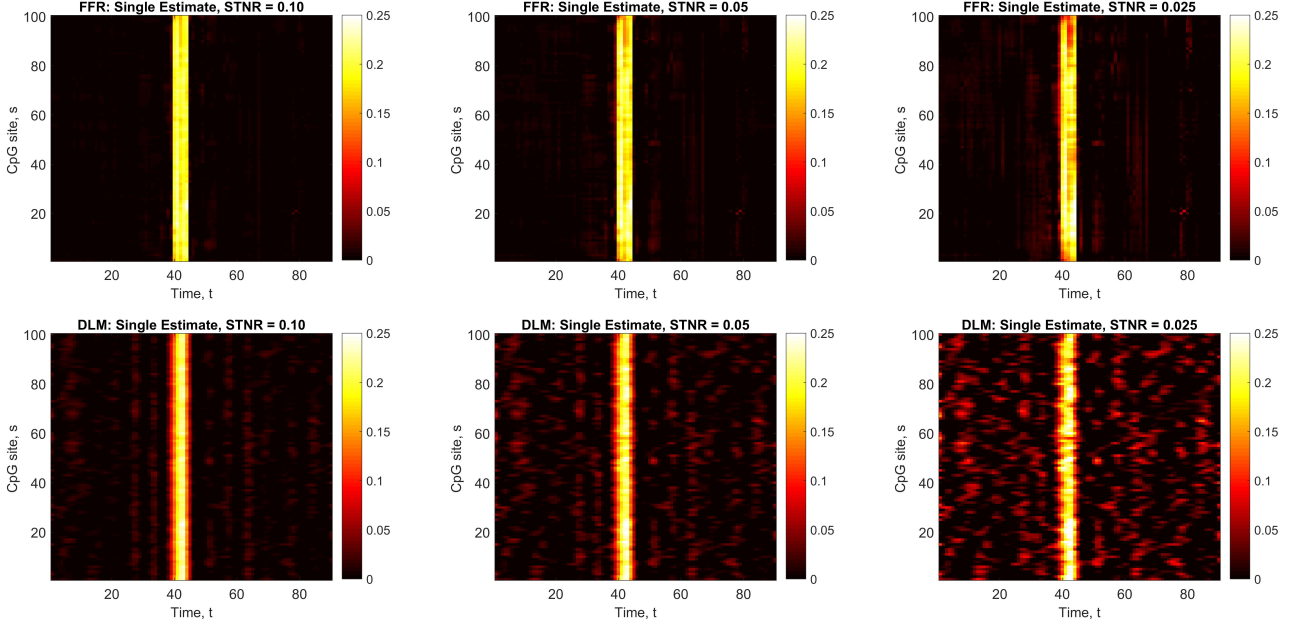


Figure 2: Heat maps of a single estimated association surface for the FFR method (top panel) and site-by-site DLM method (bottom panel).

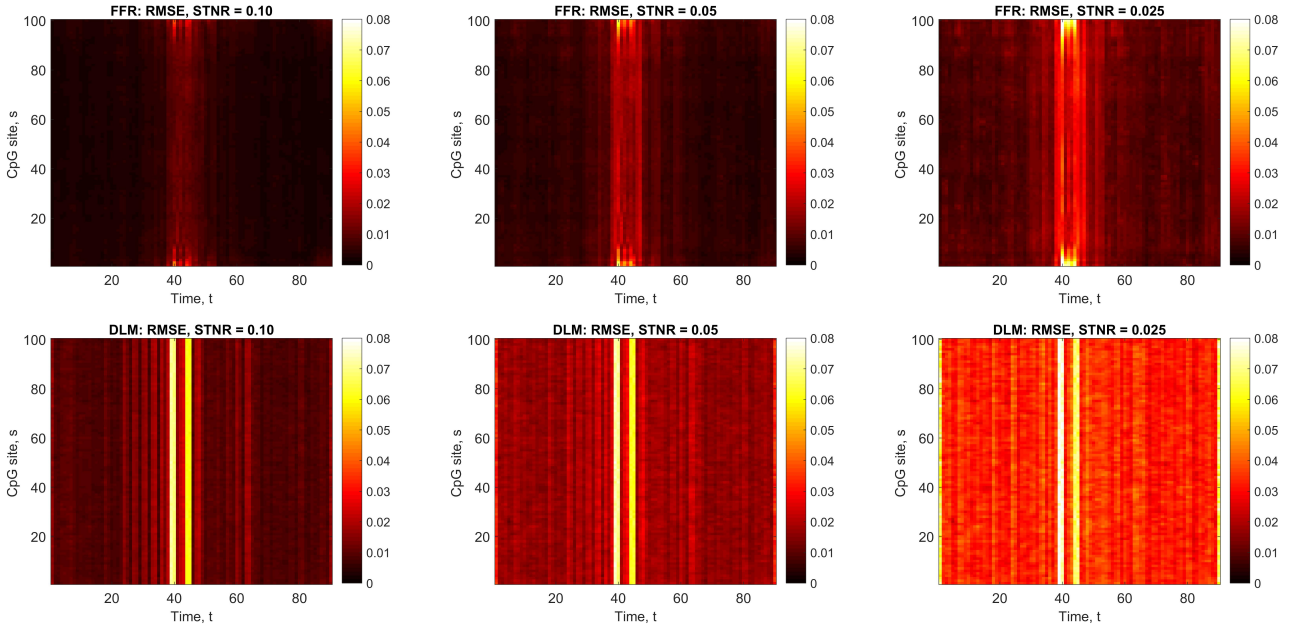


Figure 3: Heat maps displaying the RMSE averaged over 100 simulations for the FFR method (top panel) and DLM method (bottom panel).

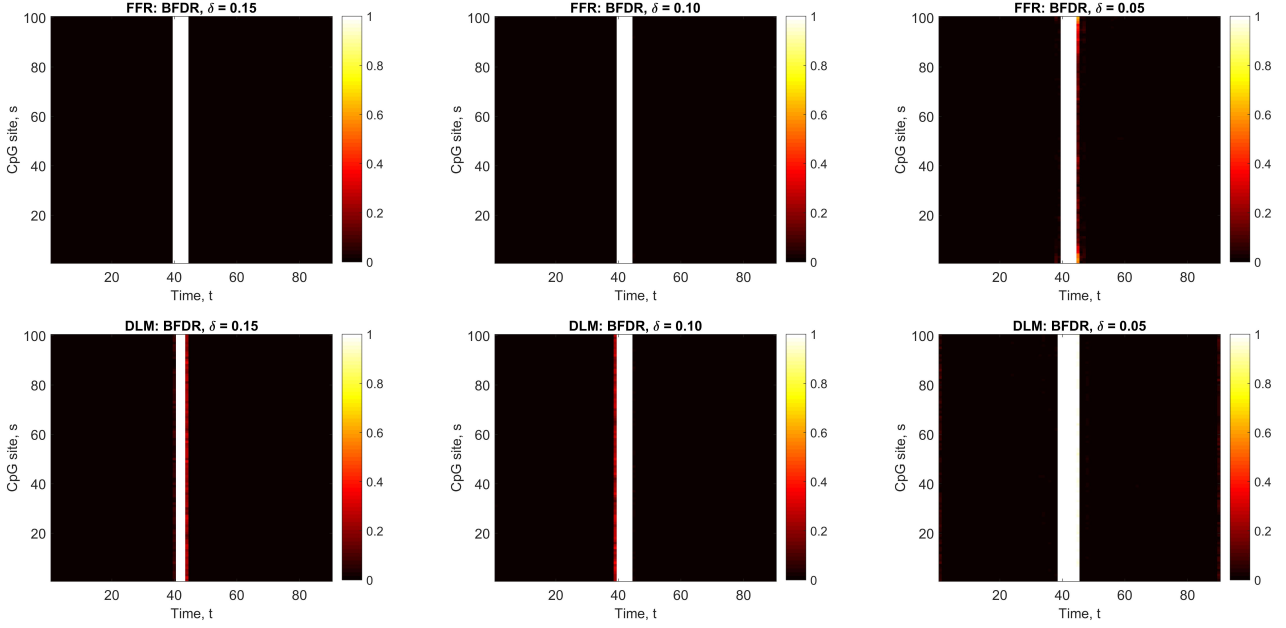


Figure 4: Heat maps of BFDR results at the  $STNR = 0.10$  level for the FFR (top panel) and DLM (bottom panel) methods averaged over 100 simulations. Left:  $\delta = 0.15$  (75% of true signal). Center:  $\delta = 0.10$  (50% of true signal). Right:  $\delta = 0.05$  (25% of true signal).

Table 1: Sensitivity and false discovery rate (FDR) for the BFDR procedure in the  $STNR = 0.10$  setting over decreasing  $\delta$  intensities.

Measure	Method	$\delta = 0.15$	$\delta = 0.10$	$\delta = 0.05$
Sensitivity	FFR	100.0%	100.0%	100.0%
	DLM	65.9%	100.0%	100.0%
FDR	FFR	0.0%	0.0%	4.7%
	DLM	0.0%	4.8%	29.9%

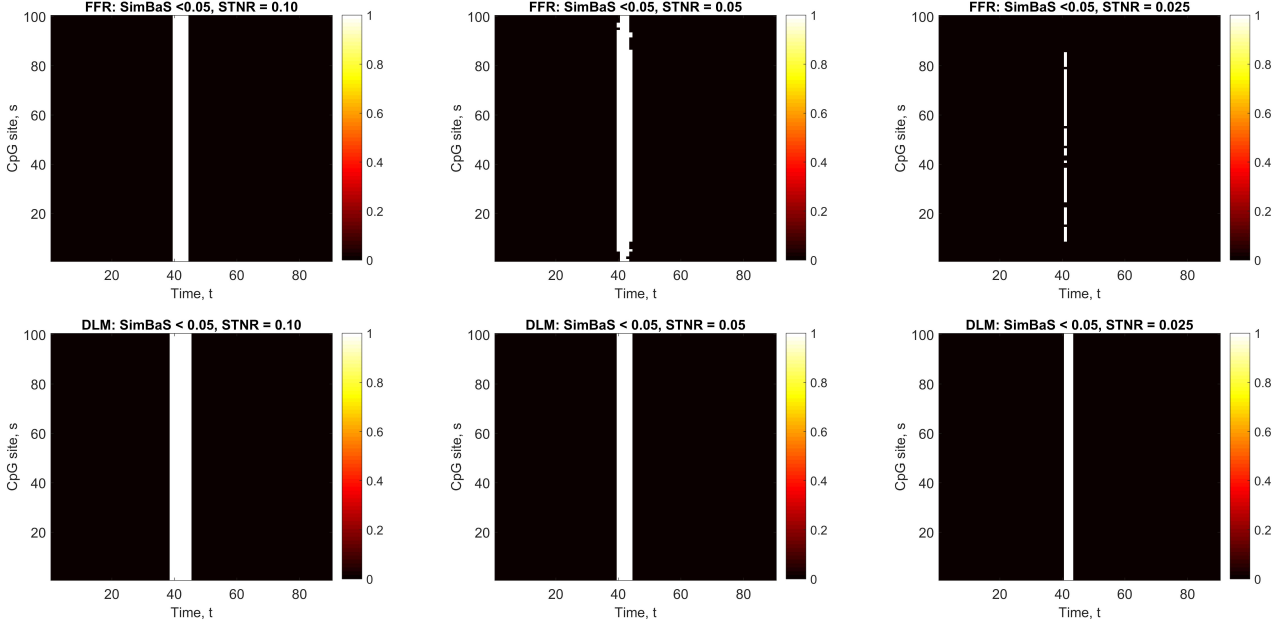


Figure 5: Heat maps of SimBaS results for the FFR (top panel) and DLM (bottom panel) methods averaged over 100 simulations and then thresholded at 0.05.

Table 2: Sensitivity and false discovery rate, FDR, for the SimBaS procedure over varying STNR settings.

Measure	Method	STNR = 0.10	STNR = 0.05	STNR = 0.025
Sensitivity	FFR	100.0%	94.4%	13.4%
	DLM	100.0%	100.0%	60.0%
FDR	FFR	0.0%	0.0%	0.0%
	DLM	28.6%	0.0%	0.0%

However, as the STNR decreases, SimBaS for FFR was more conservative than SimBaS for the DLM; when STNR = 0.025, the FFR sensitivity dropped to just 13% while the DLM maintained 60% sensitivity.

We also considered a second set of simulations for which the true association surface was a narrow, horizontal band with  $\beta = 0.2$  at probe  $s = 50$  for  $T \in \{1, \dots, 45\}$  and  $\beta = 0$  everywhere else (Figure 1; right panel). In contrast to the vertical band setting, this association surface represented a sustained window of susceptibility at a single CpG site rather than across a genomic region. Figure 6 shows the estimated surfaces, BFDR, and SimBaS heat maps for the FFR and DLM approaches at the STNR = 0.10 level. In this setting with the signal confined to a single site, the shrinkage employed by the FFR hinders its ability to identify the probe affected by exposure. The magnitude of  $\hat{\beta}_{FFR}$  in the signal region is about half the true value and the window fails to appear on either the BFDR or SimBaS plots. The DLM, however, successfully detects the true window of susceptibility for the site whose methylation is affected by exposure.

These simulations highlight the relative strengths and weaknesses of the FFR and DLM methods. For the global exposure effect setting in which an effect of exposure is shared across probes within a region of interest, FFR consistently outperforms DLM in terms of RMSE across the surface, as well as sensitivity and FDR for both the BFDR and SimBaS inferential procedures. On the other hand, for very small effect sizes (STNR = 0.025 scenario), both methods had low power, but the DLM site-by-site approach is more powerful than the FFR joint approach.

For the situation in which the window of susceptibility is localized to a single probe, the DLM site-by-site approach is more powerful than the FFR joint approach. Thus, while the FFR's ability to borrow strength across probes is beneficial when there are shared windows of susceptibility across a genomic region, the corresponding smoothing across the surface can be detrimental when the signal is sparsely distributed

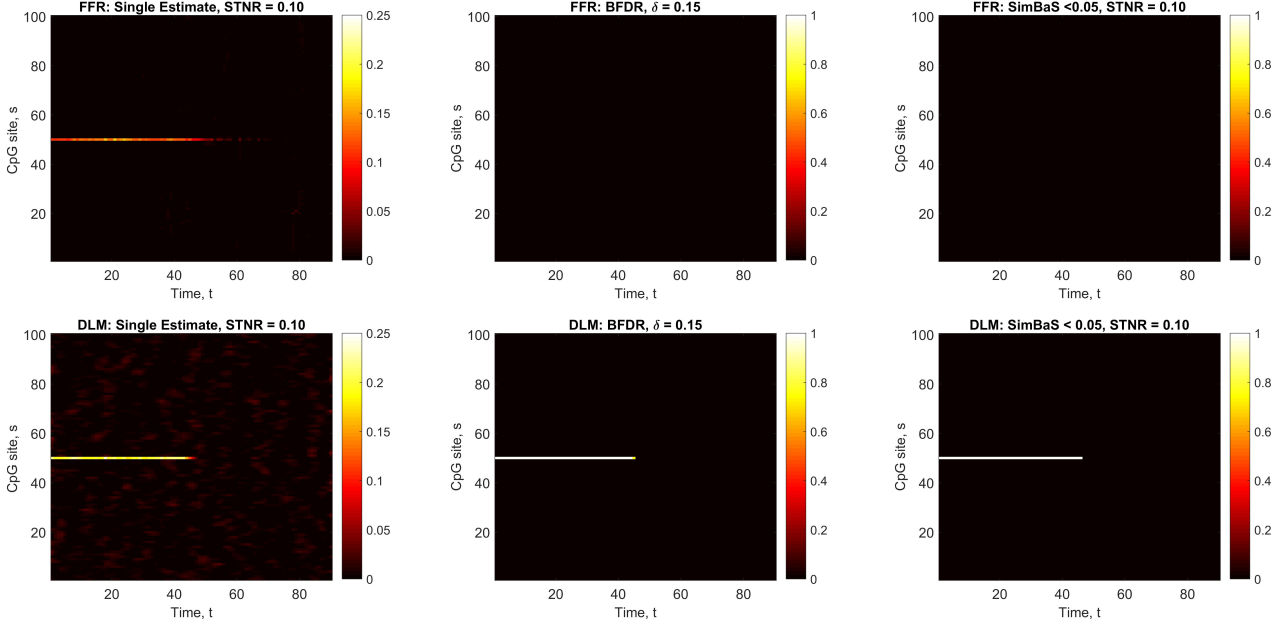


Figure 6: FFR (top panel) and DLM (bottom panel) estimated association surfaces, BFDR results for the horizontal band setting with  $STNR = 0.10$ ,  $\delta = 0.15$ , and  $\alpha = 0.05$ , and SimBaS results thresholded at 0.05.  $\beta = 0.20$  in the horizontal band signal region.

across probes or when the strength of the signal is low. These findings are unsurprising since bias-variance trade-offs are typical of shrinkage methods, particularly nonlinear shrinkage, like that used by the Bayesian FFR approach.

## 5 Results

Using data from Project Viva, our goal was to characterize the time- and position-varying association between DNA methylation levels and air pollution exposure within the last trimester of gestation. To this end, we fit Model (7) using DNA methylation level  $y(s)$ , a function of CpG site position  $s$  (relative to other CpG sites on the same chromosome) as the outcome function. The exposure function was daily maternal  $PM_{2.5}$  exposure during the 90 days prior to delivery. We included the following scalar covariates in the model: maternal BMI, race, smoking status, education level, household income, child’s race, child’s sex, gestational age, season of birth, sample plate, as well as estimated cell proportions of leukocytes (CD8+, CD4+, natural killer cells, B-lymphocytes, monocytes, granulocytes, and nucleated red blood cells).

We used Debauchies wavelets with four vanishing moments, six levels of decomposition, and zero-padding for both the outcome and predictor functions. In order to reduce the dimension of the parameter space, we performed PCA on the continuous scalar covariates and retained components that preserved 95% of their total variability. In simulation we observed that compression of the time-varying exposure led to signal distortion, so we only performed PC compression on the scalar covariates. We sampled 2000 posterior samples and discarded the first 1000.

As discussed in Section 2.2, we applied the FFR method to two regions encompassing CpG sites previously identified by Gruzjeva et al., 2019 where DNA methylation levels in cord blood were both significantly associated with PM exposure as well as implicated in respiratory-related outcomes: *FAM13A* and *NOTCH4*. Figure 8 shows the FFR- and DLM-estimated association surface for the 23 CpG probes annotated to *FAM13A* on chromosome 4. These probes span 348,819 base pairs and are labeled on the heat map according to their position relative to other CpG probes on chromosome 4 (e.g. the first CpG probe on chromosome 4 corresponds to position 1, the next CpG probe corresponds to position 2, etc.). We set  $\alpha = 0.05$  as the global BFDR bound and used  $\delta = 0.01$  as the minimum practical effect size in the BFDR calculation. The

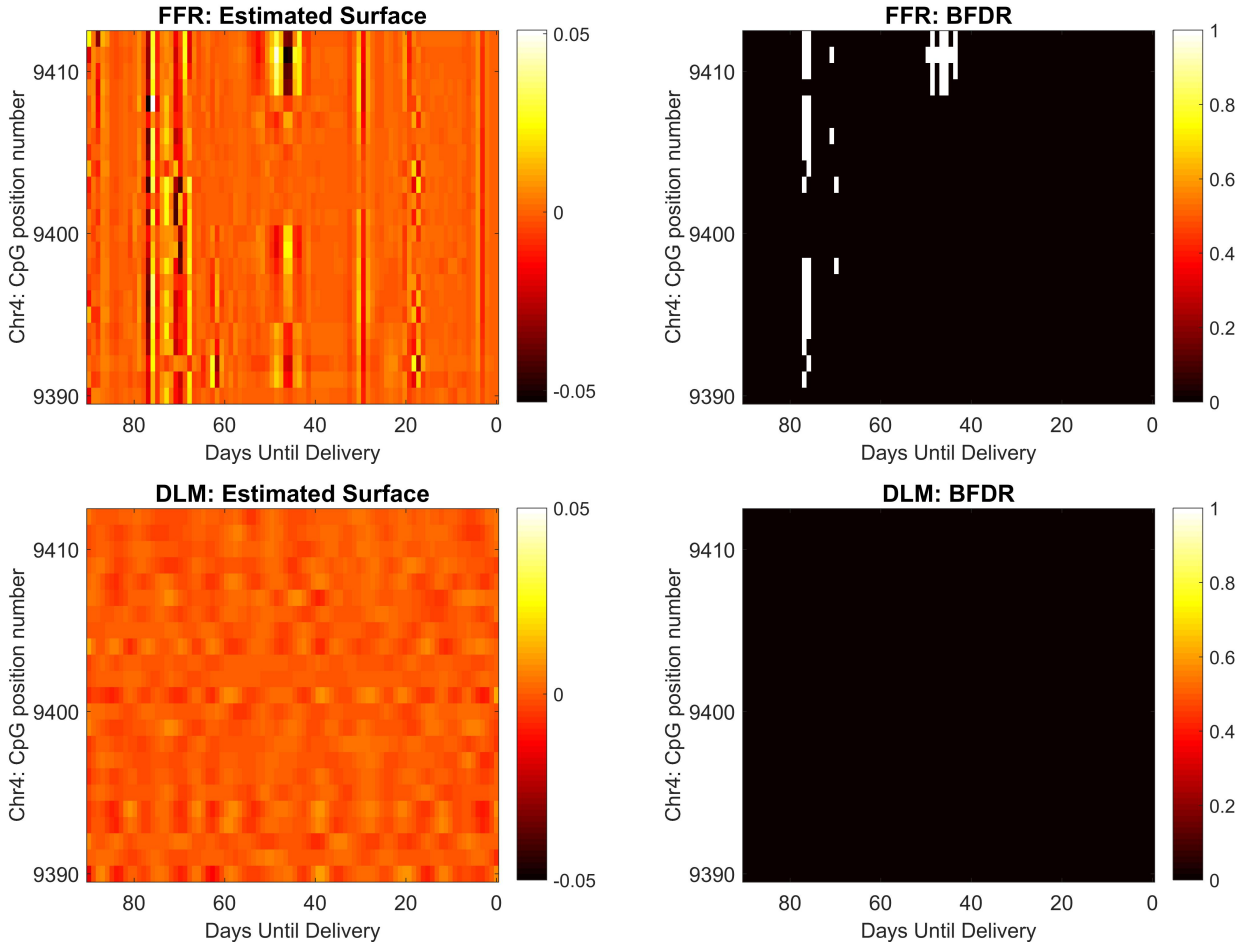


Figure 7: FFR analysis (top panel) and DLM analysis (bottom panel) for a region on chromosome 4 encompassing 23 CpG probes annotated to the *FAM13A* gene. Position numbers for each probe correspond to their position relative to other CpG probes on chromosome 4. Right panel: BFDR results with  $\delta = 0.01$  and  $\alpha = 0.05$ .

areas flagged as significant in the BFDR analysis correspond to probes in *FAM13A* coding regions and fall near the beginning of the third trimester, 78-79 days before delivery, as well as halfway through the third trimester for four probes (CpG positions 9409 - 9412 corresponding to cg17769793, cg06884401, cg25779483, cg04536922). The CpG identified by Gruzieva et al., 2019, cg00905156, corresponds to position 9402 in Figure 7. No windows of susceptibility were detected for this probe. When we performed the analogous analysis using a DLM approach, the BFDR procedure did not flag any areas of the surface.

Little is currently known about what constitutes a biologically meaningful change in methylation level, but small changes in DNA methylation in some genomic regions have been shown to have a strong effect on transcriptional activity (Breton et al., 2017); we note that in sensitivity analyses with levels of  $\delta > 0.03$ , all of the flagged regions flagged in Figure 7 disappear. The region did not appear significant when we used the SimBaS procedure to control the experiment-wise error rate.

Figure 8 shows the FFR- and DLM-estimated association surfaces for the 137 CpG probes annotated to *NOTCH4* on chromosome 6. These probes span 28,306 base pairs and are labeled according to their position relative to other CpG probes on chromosome 6. For this region, FFR finds a band of association across much of the *NOTCH4* gene 67-72 days before delivery. The CpG identified by Gruzieva et al., 2019, cg06849931, corresponds to position 11295 in Figure 8 and does not exhibit a window of susceptibility on the BFDR heat map. The corresponding BFDR image for the DLM approach does not flag any regions as

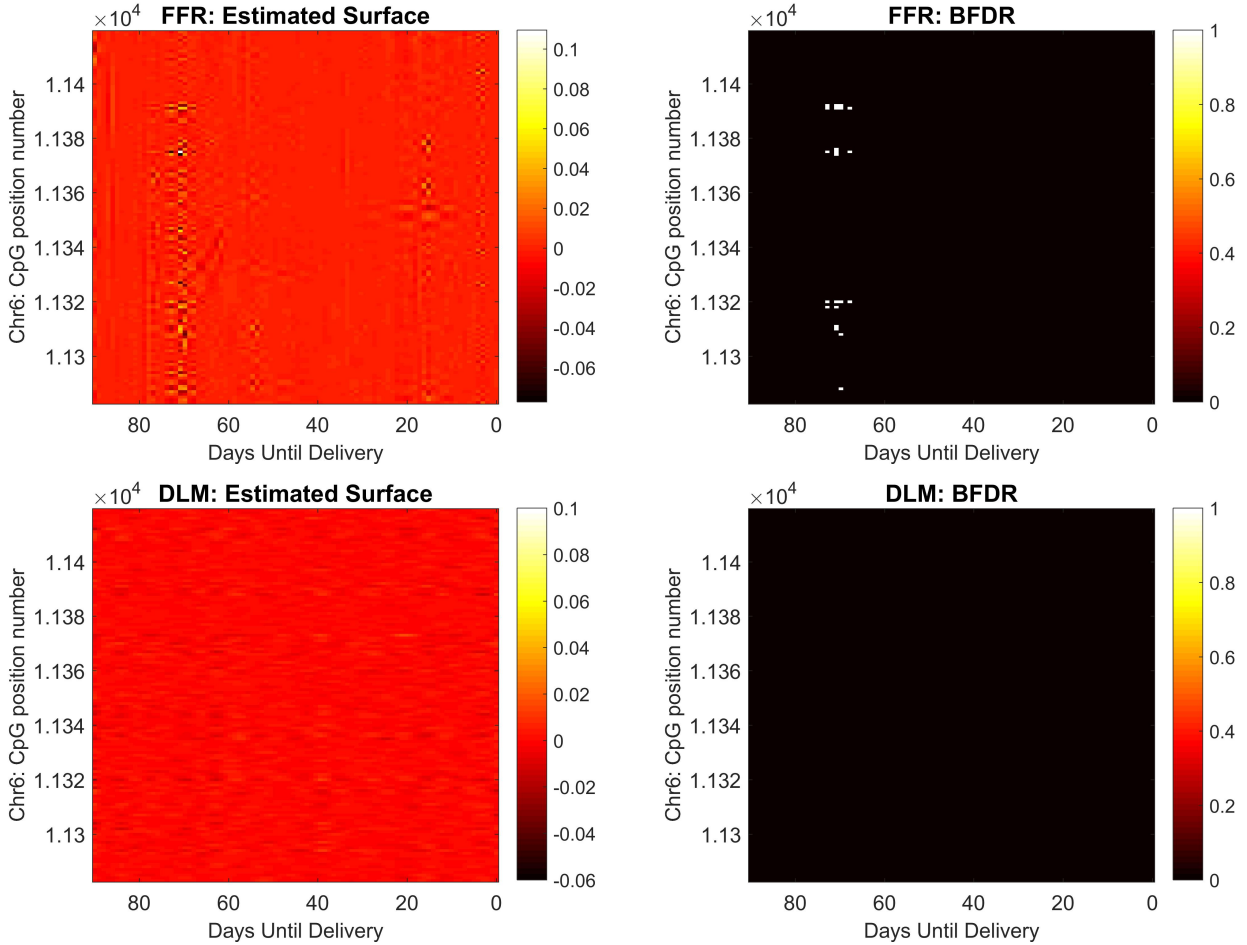


Figure 8: FFR analysis (top) and DLM analysis (bottom) for a region on chromosome 6 encompassing 137 CpG probes annotated to the *NOTCH4* gene. Position numbers for each probe correspond to their position relative to other CpG probes on chromosome 6. Right panel: BFDR results with  $\delta = 0.01$  and  $\alpha = 0.05$ .

significant, suggesting that the power gains observed in the simulation study manifested in the analysis of this genomic region as well.

## 5.1 Discussion

Functional regression is a powerful method for analyzing and visualizing associations between different sources of functional data. While a number of methods already exist for identifying differentially methylated regions and a separate body of literature addresses identifying windows of susceptibility, here we accomplish both objectives within a unified modeling framework. By enabling us to analyze associations between a spatially-varying outcome function and a time-varying exposure, functional regression provides a means of identifying differentially methylated regions exhibiting windows of susceptibility to exposures measured at a fine temporal resolution. More generally, the flexible framework presented here could be useful in a variety of high-throughput genomic applications pertaining to the transcriptome, epigenome, or metabolome. In our setting, exposure was indexed by time, but this need not be the case.

In simulation, we demonstrated that by jointly modeling epigenetic sites, FFR had greater power to identify regions associated with windows of susceptibility than the DLM approach that models sites independently. The FFR approach also maintained high sensitivity and low FDR under all but the lowest STNR scenario. In very low signal settings, the FFR lost power due to shrinkage across sites within the region of interest. This shrinkage also rendered the FFR approach less effective than the DLM at identifying windows

of susceptibility when signal was confined to a single site. Overall, the vertical and horizontal band simulation studies suggest that FFR is more effective at identifying sustained temporal effects across a genomic region, whereas a DLM is more effective at pinpointing sustained temporal effects at a spatially-localized site. In the Project Viva data analysis, FFR showed a greater ability to highlight differentially methylated regions associated with  $PM_{2.5}$  exposure during the last trimester of pregnancy than did the DLM.

Because both sustained temporal effects across genomic regions and sustained temporal effects at individual sites could be biologically significant, we recommend running both DLM and FFR analyses in a staged analytic plan. Similar to the way in which site-by-site epigenome-wide association studies are often followed by region-finding methods like DMRcate or Bumphunter, when interest focuses on finding windows of susceptibility to an exposure, we suggest performing a site-by-site DLM analysis followed by the multivariate FFR approach.

There are several limitations of our work. First, the  $PM_{2.5}$  daily measurements we used were estimated based on where the mothers enrolled in Project Viva lived, rather than by direct personal monitoring. We do not account for the prediction error from the air pollution exposure model in our inferential procedures. Second, we used wavelet basis functions in our FFR implementation since simulations showed that these worked well for the simulated surfaces that we used, but it is possible that wavelets are not the optimal basis expansion. Just as we adapted the FFR implementation of Meyer et al. (2015) to our application by removing PC compression of the exposure data in the wavelet space, additional changes to the basis expansion could be made. Future work could explore whether a different basis expansion is preferable for modeling methylation profiles and air pollution exposures. An additional limitation is that we restricted our investigation to CpG probes annotated to two genes. Our aim here was to perform the first analysis of prenatal windows of susceptibility driving the two most noteworthy associations reported by Gruzieva et al., 2019. Future work will involve a more comprehensive exploration of the genome and additional air pollutants. Identifying additional windows of susceptibility can direct attention to specific biologic mechanisms underlying associations and ultimately inform interventions to improve children’s health. This work suggests function-on-function regression is a valuable tool to achieve these objectives.

## Acknowledgements

This work was supported by NIH grants ES007142-36, ES028811, UH3 OD023286, ES000002, and US EPA grant RD-83587201. Its contents are solely the responsibility of the grantee and do not necessarily represent the official views of the USEPA. Further, USEPA does not endorse the purchase of any commercial products or services mentioned in the publication.

## References

- T. W. Anderson. *The Statistical Analysis of Time Series*. Wiley, New York, 1971.
- A. Baccarelli, R. O. Wright, V. Bollati, L. Tarantini, A. A. Litonjua, H. H. Suh, A. Zanobetti, D. Sparrow, P. S. Vokonas, and J. Schwartz. Rapid DNA methylation changes after exposure to traffic particles. *American Journal of Respiratory and Critical Care Medicine*, 179(7), 2009. ISSN 1073449X.
- V. Bollati, L. Tarantini, H. Hu, J. D. Schwartz, R. J. Wright, S. K. Park, D. Sparrow, P. S. Vokonas, A. Baccarelli, and R. O. Wright. Biomarkers of lead exposure and dna methylation within retrotransposons. *Environmental Health Perspectives*, 118(6), 2010. ISSN 0091-6765. URL <http://www.ncbi.nlm.nih.gov/pmc/articles/PMC2898855/pdf/>.
- S. Bose, Y.-H. M. Chiu, H.-H. L. Hsu, Q. Di, M. J. Rosa, A. Lee, I. Kloog, A. Wilson, J. Schwartz, R. O. Wright, S. Cohen, B. A. Coull, and R. J. Wright. Prenatal nitrate exposure and childhood asthma. influence of maternal prenatal stress and fetal sex. *American journal of respiratory and critical care medicine*, 196(11), 2017. ISSN 1073449X.
- S. Bose, M. J. Rosa, Y.-H. Mathilda Chiu, H.-H. Leon Hsu, Q. Di, A. Lee, I. Kloog, A. Wilson, J. Schwartz, R. O. Wright, W. J. Morgan, B. A. Coull, and R. J. Wright. Prenatal nitrate air pollution exposure and

- reduced child lung function: Timing and fetal sex effects. *Environmental Research*, 167:591–597, 2018. ISSN 0013-9351.
- S. Bose, K. R. Ross, M. J. Rosa, Y.-H. M. Chiu, A. Just, I. Kloog, A. Wilson, J. Thompson, K. Svensson, M. M. T. Rojo, L. Schnaas, E. Osorio-Valencia, E. Oken, R. O. Wright, and R. J. Wright. Prenatal particulate air pollution exposure and sleep disruption in preschoolers: Windows of susceptibility. *Environment international*, 124, 2019. ISSN 01604120.
- C. Breton, C. Marsit, E. Faustman, K. Nadeau, J. Goodrich, D. Dolinoy, J. Herbstman, N. Holland, J. Lasalle, R. Schmidt, P. Yousefi, F. Perera, B. Joubert, J. Wiemels, M. Taylor, I. Yang, R. Chen, K. Hew, D. Freeland, R. Miller, and S. Murphy. Small-magnitude effect sizes in epigenetic end points are important in children’s environmental health studies: The children’s environmental health and disease prevention research center’s epigenetics working group. *Environmental Health Perspectives*, 125(4):511–526, 2017. ISSN 0091-6765.
- Y.-H. M. Chiu, H.-H. L. Hsu, B. A. Coull, D. C. Bellinger, I. Kloog, J. Schwartz, R. O. Wright, and R. J. Wright. Prenatal particulate air pollution and neurodevelopment in urban children: Examining sensitive windows and sex-specific associations. *Environment International*, 87:56–65, 2016. ISSN 0160-4120.
- P. Dadvand, J. Parker, M. L. Bell, M. Bonzini, M. Brauer, L. A. Darrow, U. Gehring, S. V. Glinianaia, N. Gouveia, E.-h. Ha, J. H. Leem, E. H. van den Hooven, B. Jalaludin, B. M. Jesdale, J. Lepeule, R. Morello-Frosch, G. G. Morgan, A. C. Pesatori, F. H. Pierik, T. Pless-Mulloli, D. Q. Rich, S. Sathyanarayana, J. Seo, R. Slama, M. Strickland, L. Tamburic, D. Wartenberg, M. J. Nieuwenhuijsen, and T. J. Woodruff. Maternal exposure to particulate air pollution and term birth weight: A multi-country evaluation of effect and heterogeneity. *Environmental Health Perspectives*, 121(3), 2013. ISSN 0091-6765. URL <http://www.ncbi.nlm.nih.gov/pmc/articles/PMC3621183/pdf/>.
- L. Darrow, M. Klein, M. Strickland, J. Mulholland, and P. Tolbert. Ambient air pollution and birth weight in full-term infants in atlanta, 1994-2004. *Environmental Health Perspectives*, 119(5):731–7, 2011. ISSN 00916765. URL <http://search.proquest.com/docview/867915554/>.
- P. Du, X. Zhang, C.-C. Huang, N. Jafari, W. Kibbe, L. Hou, and S. Lin. Comparison of beta-value and m-value methods for quantifying methylation levels by microarray analysis. *BMC Bioinformatics*, 11(1): 587, 2010. ISSN 1471-2105.
- A. Fleisch, F., S. Rifas-Shiman, L., P. Koutrakis, D., J. Schwartz, A., I. Kloog, W., S. Melly, R., B. Coull, R., A. Zanobetti, R., M. Gillman, R., D. Gold, R., and E. Oken, R. Prenatal exposure to traffic pollution: Associations with reduced fetal growth and rapid infant weight gain. *Epidemiology*, 26(1):43–50, 2015. ISSN 1044-3983.
- O. Gruzieva, M. Kogevinas, J. L. Ruiz, M. Bustamante Pineda, J. M. Ant I Boqu, J. Sunyer Deu, M. Vrijheid, . Hernandez Ferrer, Carles, and E. Meln. Prenatal particulate air pollution and dna methylation in newborns: an epigenome-wide meta-analysis. *Environmental Health Perspectives*, 127(5), 2019. ISSN 0091-6765.
- S. Guo, D. Diep, N. Plongthongkum, H.-L. Fung, K. Zhang, and K. Zhang. Identification of methylation haplotype blocks aids in deconvolution of heterogeneous tissue samples and tumor tissue-of-origin mapping from plasma dna. *Nature Genetics*, 49(4):635–642, 2017. ISSN 1061-4036.
- D. B. Hancock, M. Eijgelsheim, J. B. Wilk, S. A. Gharib, L. R. Loehr, K. D. Marcante, N. Franceschini, Y. M. T. A. V. Durme, T.-H. Chen, R. G. Barr, M. B. Schabath, D. J. Couper, G. G. Brusselle, B. M. Psaty, C. M. V. Duijn, J. I. Rotter, A. G. Uitterlinden, A. Hofman, N. M. Punjabi, F. Rivadeneira, A. C. Morrison, P. L. Enright, K. E. North, S. R. Heckbert, T. Lumley, B. H. C. Stricker, G. T. O’Connor, and S. J. London. Meta-analyses of genome-wide association studies identify multiple loci associated with pulmonary function. *Nature Genetics*, 42(1):45, 2009. ISSN 1061-4036.
- M. H. Harris, D. R. Gold, S. L. Rifas-Shiman, S. J. Melly, A. Zanobetti, B. A. Coull, J. D. Schwartz, A. Gryparis, I. Kloog, P. Koutrakis, D. C. Bellinger, M. B. Belfort, T. F. Webster, R. F. White, S. K.



- Sagiv, and E. Oken. Prenatal and childhood traffic-related air pollution exposure and childhood executive function and behavior. *Neurotoxicology and Teratology*, 57:60–70, 2016. ISSN 0892-0362.
- M. Hill. Embryology fetal development, 2019. URL [https://embryology.med.unsw.edu.au/embryology/index.php/Fetal\\_Development](https://embryology.med.unsw.edu.au/embryology/index.php/Fetal_Development).
- B. D. Hobbs, K. D. Jong, M. Lamontagne, Y. Boss, N. Shrine, M. S. Artigas, L. V. Wain, I. P. Hall, V. E. Jackson, A. B. Wyss, S. J. London, K. E. North, N. Franceschini, D. P. Strachan, T. H. Beaty, J. E. Hokanson, J. D. Crapo, P. J. Castaldi, R. P. Chase, T. M. Bartz, S. R. Heckbert, B. M. Psaty, S. A. Gharib, P. Zanen, J. W. Lammers, M. Oudkerk, H. J. Groen, N. Locantore, R. Tal-Singer, S. I. Rennard, J. Vestbo, W. Timens, P. D. Par, J. C. Latourelle, J. Dupuis, G. T. O’Connor, J. B. Wilk, W. J. Kim, M. K. Lee, Y.-M. Oh, J. M. Vonk, H. J. D. Koning, S. Leng, S. A. Belinsky, Y. Tesfaigzi, A. Manichaikul, X.-Q. Wang, S. S. Rich, R. G. Barr, D. Sparrow, A. A. Litonjua, P. Bakke, A. Gulsvik, L. Lahousse, G. G. Brusselle, B. H. Stricker, A. G. Uitterlinden, E. J. Ampleford, E. R. Blecker, P. G. Woodruff, D. A. Meyers, D. Qiao, D. A. Lomas, J.-J. Yim, D. K. Kim, I. Hawrylkiewicz, P. Sliwinski, M. Hardin, T. E. Fingerlin, D. A. Schwartz, D. S. Postma, W. Macnee, M. D. Tobin, E. K. Silverman, H. M. Boezen, and M. H. Cho. Genetic loci associated with chronic obstructive pulmonary disease overlap with loci for lung function and pulmonary fibrosis. *Nature Genetics*, 49(3), 2017. ISSN 1061-4036.
- H.-H. L. Hsu, Y.-H. M. Chiu, B. A. Coull, I. Kloog, J. Schwartz, A. Lee, R. O. Wright, and R. J. Wright. Prenatal particulate air pollution and asthma onset in urban children. identifying sensitive windows and sex differences. *American journal of respiratory and critical care medicine*, 192(9), 2015. ISSN 1535-4970.
- L. Hsu, S. Self, D. Grove, T. Randolph, K. Wang, J. Delrow, L. Loo, and P. Porter. Denoising array-based comparative genomic hybridization data using wavelets. *Biostatistics*, 6(2):211–226, 2005. ISSN 1465-4644.
- I. M. Johnstone and B. W. Silverman. Wavelet threshold estimators for data with correlated noise. *Journal of the Royal Statistical Society: Series B (Statistical Methodology)*, 59(2):319–351, 1997. ISSN 1369-7412.
- I. Kloog, P. Koutrakis, B. Coull, H. Lee, and J. Schwartz. Assessing temporally and spatially resolved pm2.5 exposures for epidemiological studies using satellite aerosol optical depth measurements. *Atmospheric Environment*, 45(35):6267–6275, 2011. ISSN 1352-2310.
- I. Kloog, A. A. Chudnovsky, A. C. Just, F. Nordio, P. Koutrakis, B. A. Coull, A. Lyapustin, Y. Wang, and J. Schwartz. A new hybrid spatio-temporal model for estimating daily multi-year pm2.5 concentrations across northeastern usa using high resolution aerosol optical depth data. *Atmospheric Environment*, 95: 581–590, 2014. ISSN 1352-2310.
- D. K. Lamichhane, J. Ryu, J.-H. Leem, M. Ha, Y.-C. Hong, H. Park, Y. Kim, D.-Y. Jung, J.-Y. Lee, H.-C. Kim, and E.-H. Ha. Air pollution exposure during pregnancy and ultrasound and birth measures of fetal growth: A prospective cohort study in korea. *Science of the Total Environment*, 619-620:834–841, 2018. ISSN 0048-9697.
- E. Lavigne, J. Donelle, M. Hatzopoulou, K. Van Ryswyk, A. van Donkelaar, R. V. Martin, H. Chen, D. M. Stieb, A. Gasparrini, E. Crighton, A. S. Yasseen, R. T. Burnett, M. Walker, and S. Weichenthal. Spatiotemporal variations in ambient ultrafine particles and the incidence of childhood asthma. *American journal of respiratory and critical care medicine*, 199(12), 2019. ISSN 1073449X.
- A. Lee, B. Legrand, H. Hsu, Y. Chiu, K. Brennan, S. Bose, M. Rosa, I. Kloog, A. Wilson, J. Schwartz, W. Morgan, B. Coull, R. Wright, A. Baccarelli, and R. Wright. Prenatal fine particulate exposure associated with reduced childhood lung function and nasal epithelia gstp1 hypermethylation: Sex-specific effects. *American Journal Of Respiratory And Critical Care Medicine*, 197, 2018. ISSN 1073-449X.
- K. H. Lee, M. G. Tadesse, A. A. Baccarelli, J. Schwartz, and B. A. Coull. Multivariate bayesian variable selection exploiting dependence structure among outcomes: Application to air pollution effects on dna methylation. *Biometrics*, 73(1):232–241, 2017. ISSN 0006-341X.
- W. Lee and J. S. Morris. Identification of differentially methylated loci using wavelet-based functional mixed models. *Bioinformatics*, 32(5):664–672, 2016. ISSN 1367-4803.

- J. Lepeule, A. Baccarelli, L. Tarantini, V. Motta, L. Cantone, A. A. Litonjua, D. Sparrow, P. S. Vokonas, and J. Schwartz. Gene promoter methylation is associated with lung function in the elderly: The normative aging study. *Epigenetics*, 7(3):261–269, 2012. ISSN 1559-2294.
- X. Li, G. A. Hawkins, E. J. Ampleford, W. C. Moore, H. Li, A. T. Hastie, T. D. Howard, H. A. Boushey, W. W. Busse, W. J. Calhoun, M. Castro, S. C. Erzurum, E. Israel, R. F. Lemanske, S. J. Szefer, S. I. Wasserman, S. E. Wenzel, S. P. Peters, D. A. Meyers, and E. R. Bleeker. Genome-wide association study identifies th1 pathway genes associated with lung function in asthmatic patients. *The Journal of Allergy and Clinical Immunology*, 132(2):313–320.e15, 2013. ISSN 0091-6749.
- E. J. Malloy, J. S. Morris, S. D. Adar, H. Suh, D. R. Gold, and B. A. Coull. Wavelet-based functional linear mixed models: an application to measurement errorcorrected distributed lag models. *Biostatistics*, 11(3):432–452, 2010. ISSN 1465-4644.
- M. J. Meyer, B. A. Coull, F. Versace, P. Cinciripini, and J. S. Morris. Bayesian functiononfunction regression for multilevel functional data. *Biometrics*, 71(3):563–574, 2015. ISSN 0006-341X.
- J. Morris and R. Carroll. Wavelet-based functional mixed models. *Journal Of The Royal Statistical Society Series B-Statistical Methodology*, 68:179–199, 2006. ISSN 1369-7412.
- J. S. Morris, P. J. Brown, R. C. Herrick, K. A. Baggerly, and K. R. Coombes. Bayesian analysis of mass spectrometry proteomic data using waveletbased functional mixed models. *Biometrics*, 64(2):479–489, 2008. ISSN 0006-341X.
- P. Müller, G. Parmigiani, V. C. Rice, I. Fernández-Val, and A. Kowalski. FDR and Bayesian multiple comparison rules. Working paper, 2006.
- E. Oken, A. A. Baccarelli, D. R. Gold, K. P. Kleinman, A. A. Litonjua, D. De Meo, J. W. Rich-Edwards, S. L. Rifas-Shiman, S. Sagiv, E. M. Taveras, S. T. Weiss, M. B. Belfort, H. H. Burris, C. A. Camargo, S. Y. Huh, C. Mantzoros, M. G. Parker, and M. W. Gillman. Cohort profile: Project viva. *International Journal of Epidemiology*, 44(1):37–48, 2015. ISSN 0300-5771.
- M. P. R. J. Ruppert, David;Wand. *Semiparametric Regression*. Cambridge University Press, Cambridge, 2003. ISBN 9780521780506.
- S. Sardy, D. Percival, A. Bruce, H.-Y. Gao, and W. Stuetzle. Wavelet shrinkage for unequally spaced data. *Statistics and Computing*, 9(1):65–75, 1999. ISSN 0960-3174.
- J. Schneider, S. Kidd, and D. Anderson. Influence of developmental lead exposure on expression of dna methyltransferases and methyl cytosine-binding proteins in hippocampus. *Toxicology Letters*, 217(1):75–81, 2013. ISSN 0378-4274.
- J. Schwartz. The distributed lag between air pollution and daily deaths. *Epidemiology*, 11(3):320–326, 2000. ISSN 1044-3983.
- P. S. Shah and T. Balkhair. Air pollution and birth outcomes: A systematic review. *Environment International*, 37(2):498–516, 2011. ISSN 0160-4120.
- S. Soberanes, A. Gonzalez, D. Urich, S. E. Chiarella, K. A. Radigan, A. Osornio-Vargas, J. Joseph, B. Kalyanaraman, K. M. Ridge, N. S. Chandel, G. M. Mutlu, A. D. Vizcaya-Ruiz, and G. R. S. Budinger. Particulate matter air pollution induces hypermethylation of the p16 promoter via a mitochondrial ros-jnk-dnmt1 pathway. *Scientific Reports*, 2(1), 2012. ISSN 20452322.
- J. E. Sordillo, S. L. Rifas-Shiman, K. Switkowski, B. Coull, H. Gibson, M. Rice, T. A. E. Platts-Mills, I. Kloog, A. A. Litonjua, D. R. Gold, and E. Oken. Prenatal oxidative balance and risk of asthma and allergic disease in adolescence. *The Journal of allergy and clinical immunology*, 2019. ISSN 00916749. URL <http://search.proquest.com/docview/2295474755/>.

- L. van Rossem, S. L. Rifas-Shiman, S. J. Melly, I. Kloog, H. Luttmann-Gibson, A. Zanobetti, B. A. Coull, J. D. Schwartz, M. A. Mittleman, E. Oken, M. W. Gillman, P. Koutrakis, and D. R. Gold. Prenatal air pollution exposure and newborn blood pressure. *Environmental Health Perspectives*, 123(4), 2015. ISSN 0091-6765. URL <http://www.ncbi.nlm.nih.gov/pmc/articles/PMC4384198/pdf/>.
- J. L. Warren, W. Kong, T. J. Luben, and H. H. Chang. Critical window variable selection: estimating the impact of air pollution on very preterm birth. *Biostatistics (Oxford, England)*, 2019. ISSN 14654644.
- A. Wilson, Y.-H. M. Chiu, H.-H. L. Hsu, R. O. Wright, R. J. Wright, and B. A. Coull. Bayesian distributed lag interaction models to identify perinatal windows of vulnerability in childrens health. *Biostatistics*, 18(3):537–552, 2017. ISSN 1465-4644.
- H. Wu, B. Jiang, P. Zhu, X. Geng, Z. Liu, L. Cui, and L. Yang. Associations between maternal weekly air pollutant exposures and low birth weight: a distributed lag non-linear model. *Environmental Research Letters*, 13(2), 2018. ISSN 1748-9326.
- A. Zanobetti, M. P. Wand, J. Schwartz, and L. M. Ryan. Generalized additive distributed lag models: quantifying mortality displacement. *Biostatistics*, 1(3):279–292, 2000. ISSN 1465-4644.

## Appendices

### A Additional Simulation Results

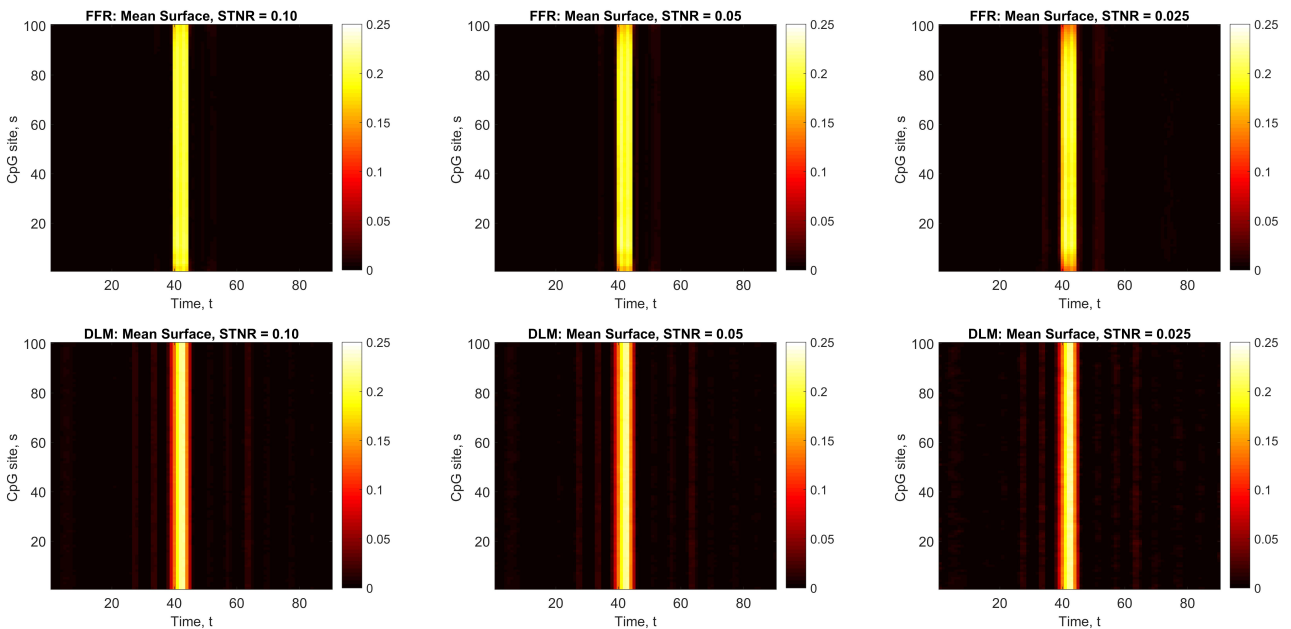


Figure 9: Heat maps of the estimated surface averaged over 100 datasets. Top panel: FFR estimates. Bottom panel: DLM estimates concatenated across the surface.

## B $PM_{2.5}$ exposure

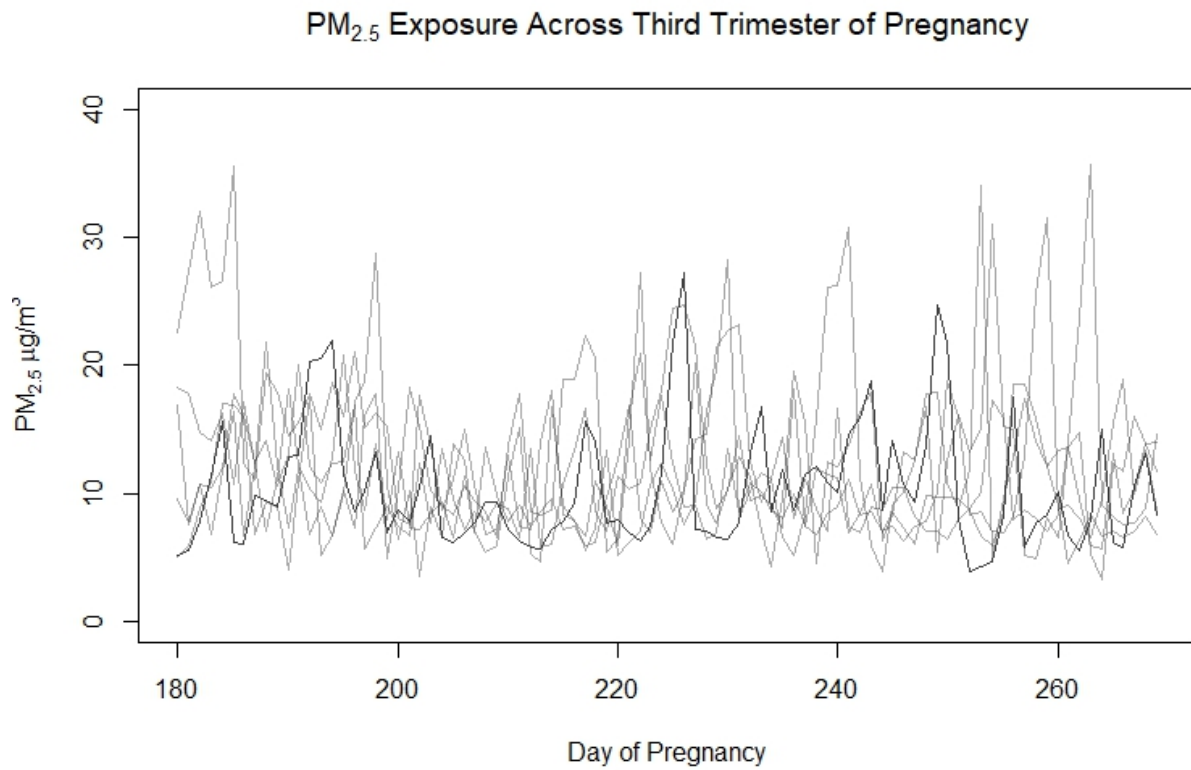


Figure 10:  $PM_{2.5}$  exposure over the third trimester of pregnancy for a randomly selected subject in Project Viva (black) and five additional subjects (grey).